Joint Detection and Recognition of Satellites' Orientated Components with Compact Polarimetric ISAR

Ming-Dian Li[(1)], Xing-Chao Cui[(1)], Shun-Ping Xiao[(1)], and Si-Wei Chen*[(1)]
(1) College of Electronic Science and Technology, National University of Defense Technology, Changsha, China
*chenswnudt@163.com

Abstract

Compared with optical imaging system, polarimetric inverse synthetic aperture radar (ISAR) can work all day and all-weather, which plays an important role in space surveillance. Accurate identification of the structural components of man-made targets can yield valuable information for distinguishing target behaviors. In this vein, an anchor-free orientated component detector is established. The orientated bounding box of target component is modeled by a 2-D Gaussian distribution. Consequently, the angle, center point position and size parameters can be coupled for joint optimization. Additionally, since there is lack of public dataset available, compact polarimetric ISAR orientated component annotation datasets are constructed for five satellites. The experimental results demonstrate the better performance for the proposed method with the mean average precision (mAP) index of 0.618.

1. Introduction

ISAR is capable of observing space target by transmitting a large bandwidth electromagnetic wave [1], of which polarization is an essential property [2-6]. The compact polarimetric (CP) mode is a unique dual-polarization mode, which balances the hardware costs and polarization information [7]. Among compact polarimetric, Dual Circular Polarimetric (DCP) mode is considered.

The fine-grained detection and recognition of radar target components is of significance for distinguishing target types and analyzing target behavior. For the challenges of multi-target and multi-scale target detection, boxes or points are generally pre-initialized, and the residual between the initial and the ground-truth is regressed on this basis. These two methods are referred to as anchor-based [8, 9] and anchor-free [10, 11], respectively. Compared with horizontal object detection, the attribute information such as target orientation and aspect ratio can be obtained for orientated object detection [12]. However, optimizing angle, position and size information separately may not yield ideal performance, which makes joint optimization a worthwhile consideration. In summary, the main contributions of this paper are listed as follows:

- Orientated components detection and recognition datasets of compact polarimetric ISAR images for satellites are constructed. Fine-grained component-level annotations with angle information are included for radar targets.
- An anchor-free orientated component detector with joint optimization of angle, position and size parameters is established.

2. Joint Optimization Model for Compact Polarimetric ISAR Component Detection

2.1 Basic of Compact Polarimetric ISAR in DCP Mode

Compact polarization indicates the possibility of reducing the complexity, cost, and data rate of a radar system [13]. For the DCP mode, without any loss, the transmitting antenna operates with left-hand circular polarization, while the receiving antennas operate with both left-hand and right-hand circular polarizations. In this vein, the compact polarimetric scattering vector is as $\mathbf{k}_{\mathrm{DCP}} = \left[S_{\mathrm{LL}} \quad S_{\mathrm{RL}}\right]^{\mathrm{T}}$, where the superscript T indicates the transpose operation. The subscript RL refers to left-hand circular polarization transmitting and right-hand circular polarization receiving. The other is defined similarly. To make full use of the complex information, the compact polarimetric ISAR image data is represented by four real terms as

$$I = \left[\mathrm{Re}\left(S_{\mathrm{LL}}\right), \mathrm{Im}\left(S_{\mathrm{LL}}\right), \mathrm{Re}\left(S_{\mathrm{RL}}\right), \mathrm{Im}\left(S_{\mathrm{RL}}\right)\right]^{\mathrm{T}} \tag{1}$$

where $\mathrm{Re}(\bullet)$ and $\mathrm{Im}(\bullet)$ denote the real and imaginary parts, respectively and $I \in \mathbb{R}^{4\times H\times W}$.

2.2 Joint Optimization Model for Parameter Estimation

The center coordinates of n th component ς_c^n in c th type is as (x, y). Rectangle bounding box with orientation angle θ of ς_c^n is considered and the length and width are (h, w). The parameters to be estimated are (x, y, h, w, θ, c). Unlike the classical detector [8, 9], (x, y, h, w, θ, c) are jointly estimated and solved. Inspirer by [14], the orientated bounding box is modeled by a 2-D Gaussian distribution $\mathcal{N}(\boldsymbol{\mu}, \boldsymbol{\Sigma})$ shown in Fig. 1, as

$$\boldsymbol{\mu} = (x, y)^{\mathrm{T}} \tag{2}$$

$$
\begin{aligned}
\boldsymbol{\Sigma}^{1/2} &= \mathbf{RMR}^{\mathrm{T}} \\
&= \begin{pmatrix} \cos\theta & -\sin\theta \\ \sin\theta & \cos\theta \end{pmatrix} \begin{pmatrix} \frac{w}{2} & 0 \\ 0 & \frac{h}{2} \end{pmatrix} \begin{pmatrix} \cos\theta & \sin\theta \\ -\sin\theta & \cos\theta \end{pmatrix} \\
&= \begin{pmatrix} \frac{w}{2}\cos^2\theta + \frac{h}{2}\sin^2\theta & \frac{w-h}{2}\cos\theta\sin\theta \\ \frac{w-h}{2}\cos\theta\sin\theta & \frac{w}{2}\sin^2\theta + \frac{h}{2}\cos^2\theta \end{pmatrix}
\end{aligned} \tag{3}
$$

where the orientation matrix is $\mathbf{R}$. Points $\mathbf{P}_t$ in the ground-truth oriented bounding box obeys distribution $\mathcal{N}_t(\boldsymbol{\mu},\boldsymbol{\Sigma})$, while $\mathbf{P}_e \sim \mathcal{N}_e(\boldsymbol{\mu},\boldsymbol{\Sigma})$ is satisfied for points $\mathbf{P}_e$ in the estimated orientated bounding box. The optimization goal is to make $\mathcal{N}_e(\boldsymbol{\mu},\boldsymbol{\Sigma})$ and $\mathcal{N}_t(\boldsymbol{\mu},\boldsymbol{\Sigma})$ coincide as much as possible. In order to measure the distance between the two, Kullback-Leibler divergence (KLD) [15] is adopted and for the 2-D Gaussian distribution, the KLD result $\mathbf{D}\left(\mathcal{N}_e \,\|\, \mathcal{N}_t\right)$ is

$$
\begin{aligned}
&\mathbf{D}\left(\mathcal{N}_e \,\|\, \mathcal{N}_t\right) \\
&= \frac{1}{2}\left(\boldsymbol{\mu}_e - \boldsymbol{\mu}_t\right)^{\mathrm{T}} \boldsymbol{\Sigma}_t^{-1}\left(\boldsymbol{\mu}_e - \boldsymbol{\mu}_t\right) + \frac{1}{2}\mathrm{Tr}\left(\boldsymbol{\Sigma}_t^{-1}\boldsymbol{\Sigma}_e\right) + \frac{1}{2}\ln\frac{\left|\boldsymbol{\Sigma}_t\right|}{\left|\boldsymbol{\Sigma}_e\right|} - 1
\end{aligned} \tag{4}
$$

A detection branch and a recognition branch are utilized to simultaneously estimated the parameters (x, y, h, w, θ) and class parameter c, where the feature extraction procedure is shared. In this vein, all the five parameters are jointly predicted.

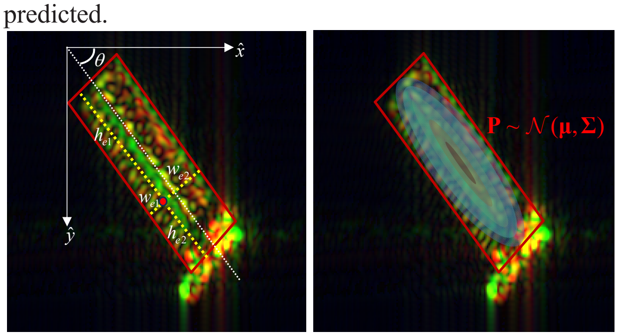

(a) (b)

Fig. 1 Illustrations of the bounding box representation for component in compact polarimetric ISAR image with pseudo-color (R: $\left|S_{\mathrm{RL}}\right|$, G: $\left|S_{\mathrm{LL}}\right|$, B: $\mathrm{Arg}\left(S_{\mathrm{LL}}S_{\mathrm{RL}}^{*}\right)$). (a) Orientated bounding box representation in Euclidean distance for anchor-free framework. (b) Orientated bounding box representation in 2-D Gaussian distribution.

2.3 Single Stage Anchor-Free Detector for Orientated Components Detection and Recognition

The original optimization goal is to minimize the distance $(\Delta x, \Delta y, \Delta h, \Delta w, \Delta\theta, \Delta c)$ between the estimation and the ground-truth, while it is $\min\left[\mathbf{D}\left(\mathcal{N}_e \,\|\, \mathcal{N}_t\right)\right]$ for the 2-D Gaussian distribution representation. The prior information is usually utilized for position parameter initialization, which is anchor point sets for the anchor-free detector. The ground-truth biases between the prior information $\left(x_p, y_p, h_p, w_p, \theta_p\right)$ and the ground-truth bounding box are $\left(b_x^t, b_y^t, b_h^t, b_w^t, b_\theta^t\right)$. In the anchor-free framework [10], distance between the anchor point $\left(x_p, y_p\right)$ and four edges of the ground-truth is utilized for optimization. The estimated distance value is defined as $\left(h_{e1}, h_{e2}, w_{e1}, w_{e2}\right)$ and shown in Fig. 1 (a). The red rectangle denotes the predicted orientated bounding box and the red point represents the anchor point $\left(x_p, y_p\right)$, which is the only prior information. Note that $\left(x_e, y_e\right)$ is the center point's coordinate of the predicted anchor box in Fig. 1 (a) and the following equations hold as

$$
\begin{aligned}
\Delta x &= x_e - x_t = x_p + b_x^e - x_t = b_x^t + b_x^e \\
&= b_x^t + \left(\frac{w_{e1} - w_{e2}}{2}\right)\sin\theta_e + \left(\frac{h_{e1} - h_{e2}}{2}\right)\cos\theta_e
\end{aligned} \tag{5}
$$

$$
\begin{aligned}
\Delta y &= x_e - x_t = x_p + b_x^e - x_t = b_x^t + b_x^e \\
&= b_y^t + \left(\frac{h_{e1} - h_{e2}}{2}\right)\sin\theta_e - \left(\frac{w_{e1} - w_{e2}}{2}\right)\cos\theta_e
\end{aligned} \tag{6}
$$

$$
h_e = h_{e1} + h_{e2}, w_e = w_{e1} + w_{e2} \tag{7}
$$

In this vein, for the anchor-free detector in single stage, elements in equation (4) can be calculated. The algorithm flow chart is shown in Fig. 2. The ResNet with cross stage partial module called CSPNET [11] is utilized as the backbone for multi-level feature extraction and fusion. Then, two branches with fully convolution layer are established to predict parameters $\left(h_{e1}, h_{e2}, w_{e1}, w_{e2}\right)$ and class parameter c, separately. In order to jointly optimize these parameters, the quality focal loss in is also adopted. The cross-entropy loss can be weighed by the IOU score calculated by the detection branch.

3. Construction of Compact Polarimetric ISAR Component Detection and Recognition Dataset

The Chinese HISEA-1 satellite, StarLink satellite, Capella satellite, QPS-SAR satellite and the Worldview-4 satellite are adopted for investigation. The fine models are shown in Fig. 3. The compact polarimetric ISAR echoes are collected using the electromagnetic simulation method [16] under 91 azimuth perspectives, while the elevation angles are set as 40° and 45°, respectively. The image datasets are constructed using 5° synthetic aperture and 2GHz bandwidth in Ku band. Through FFT interpolation, the pixel size of each ISAR image frame is 256×256 and the data augmentations of random flip and random rotation are adopted.

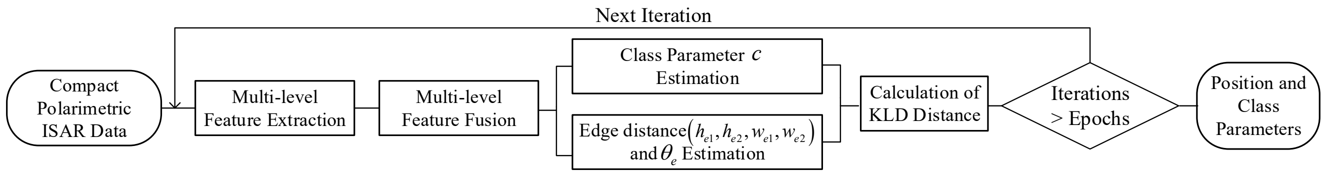

Fig. 2. The algorithm flow chart.

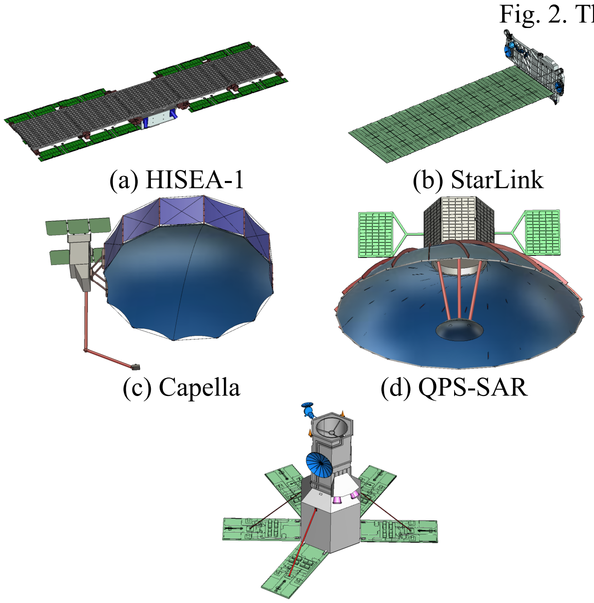

(a) HISEA-1 (b) StarLink

(c) Capella (d) QPS-SAR

(e) Worldview-4

Fig. 3. Fine CAD model of five satellites.

The point clouds of the satellites' components are labeled first. The details can be found in our previous work [17]. Considering the function and geometric shape, fifteen components are considered in combination with the ISAR imaging results in Table I. Then, the 3-D labelling information is projected into the imaging plane using the imaging geometric relationship and the occlusion between the components is also considered. Finally, based on the projection point sets, the orientated bounding box with angle information can be generated, which are shown in Fig. 1 (a). The mean value of component size at different elevation angles are listed in Table I. The components in satellites can be multi-scale and multi-ratio. Some components have the characteristics of long and narrow distribution, such as the supporting arm.

4. Experiments

The whole datasets are divided into training, validation, and test datasets in a ratio of 6:2:2. Datasets containing samples in 40° and 45° elevation angles are defined as λ^{40} and λ^{45}, respectively. The rotated faster R-CNN method [8], oriented R-CNN method [9], PSC method [10] and RTMdet method [11] for orientation object, are adopted for comparison. All approached are trained using $\lambda^{40}_{\text{train}}$ and $\lambda^{45}_{\text{train}}$, respectively and tested with $\lambda^{40}_{\text{test}}$ and $\lambda^{45}_{\text{test}}$, respectively. Limited to the paper length, part of the detection and recognition results in 45 ° elevation angle are depicted in Fig. 4. The mean average precision (mAP) index [9] with 0.5 threshold is adopted and calculated among all 15 components for quantitative evaluation, which are shown in Table II and Table III. It can be observed that the proposed method is better over the two training datasets. The mean mAP index for the proposed approach achieves 0.618, which is 0.049 higher than the best one and 0.093 higher than the lowest one.

TABLE I. MEAN VALUE OF COMPONENT SIZE AT DIFFERENT ELEVATION ANGLES

Component Type	**Component Name**	**Mean Size (Pixel)**	
		40°	45°
Body	Cuboid body	148	139
	Polygon body	1463	1445
	Plate body	2775	2723
Solar array	Solar array	1216	1439
Antenna	Parabolic antenna surface	5464	6328
	Parabolic antenna part	452	522
	Panel antenna	4063	4845
	Cone antenna	22	23
Fitting	Plate fitting	18	19
	Rod fitting	373	385
Sensor	Sensor	21	21
Supporting structure	Rod supporting arm	130	123
	Plate supporting arm	165	166
Optical lens	Polygon optical lens	1598	1740
Propulsion	Propulsion	296	315

5. Conclusion

An anchor-free orientated component detector is established in this work. 2-D Gaussian distribution is utilized for modeling the bounding box of the target component, which facilitates the joint optimization of angle, center point position and size parameters. Besides, compact polarization ISAR fine-grained orientated component annotation datasets are constructed for five satellites. The distribution of the components' size, length-to-width ratio and orientation angle value are also analyzed. Based on this, anchor-based and anchor-free detectors are adopted for comparison. The experimental results demonstrate the better performance for the proposed method, with the mAP index of 0.618. However, further investigations are needed to improve the detection performance of components with small area, large length-to-width ratio and weak scattering power.

6. Acknowledgment

This work was supported in part by the National Natural Science Foundation of China under Grant 62122091. The authors would like to thank the deviation of OpenMMLab for the designed mmrotate platform.

TABLE II. QUANTITATIVE RESULTS WITH λ_{train}^{40} TRAINING

Type	Method	mAP@50		Mean Value
		40°	45°	
Anchor-based	rotated faster R-CNN	0.613	0.526	0.570
	oriented R-CNN	0.620	0.471	0.546
Anchor-free	PSC	0.611	0.440	0.526
	RTMdet	0.615	0.508	0.562
	Proposed	**0.674**	**0.540**	**0.607**

TABLE III. QUANTITATIVE RESULTS WITH λ_{train}^{45} TRAINING

Type	Method	mAP@50		Mean Value
		40°	45°	
Anchor-based	rotated faster R-CNN	0.511	0.625	0.568
	oriented R-CNN	0.476	0.572	0.524
Anchor-free	PSC	0.454	0.597	0.526
	RTMdet	0.428	0.556	0.492
	Proposed	**0.581**	**0.677**	**0.629**

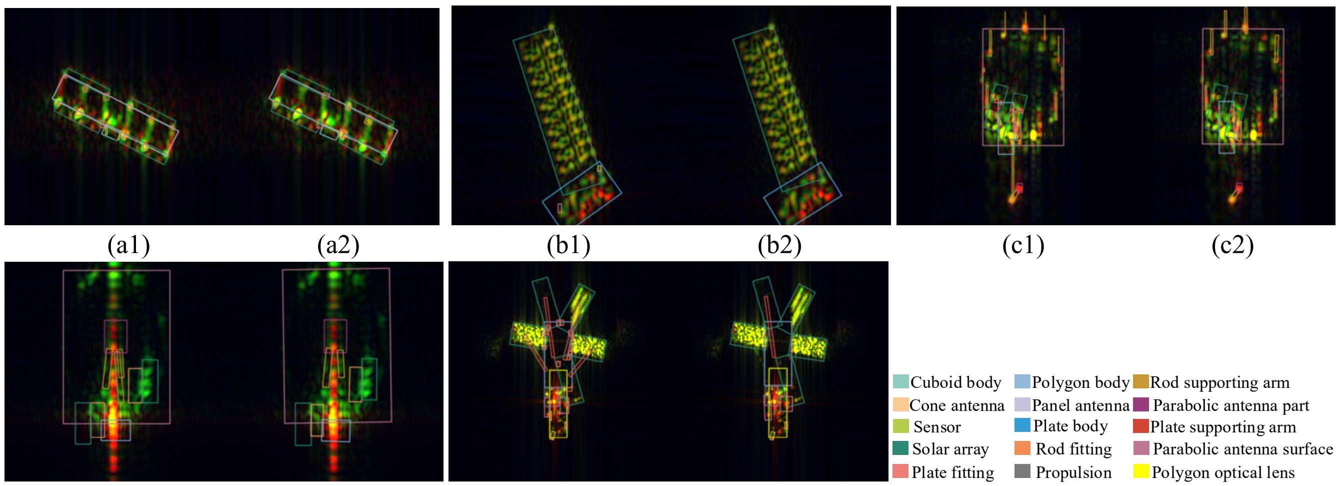

Fig. 4.Part of the detection and recognition results in 45° elevation angle for five satellites. Different components are labeled with different colors. Number 1 stands for the ground-truth, while number 2 indicates the prediction results. (a)-(e) represent the HISEA-1, StarLink, Capella, QPS-SAR and Worldview-4 satellites, respectively.

References

[1] X. C. Cui, Y. W. Fu, Y. Su, and S. W. Chen, "Physical Parameters Joint Estimation of Satellite Parabolic Antenna With Key Frame Pol-ISAR Images," *IEEE Trans. Geosci. Remote Sens.*, vol. 62, pp. 1-16, 2024.

[2] S. Chen, M. Li, X. Cui, and H. Li, "Polarimetric roll-invariant features and applications for polarimetric synthetic aperture radar ship detection: A comprehensive summary and investigation," *IEEE Geosci. Remote Sens. Mag.*, pp. 1-32, 2023.

[3] M. D. Li, S. P. Xiao, and S. W. Chen, "Three-Dimension Polarimetric Correlation Pattern Interpretation Tool and its Application," *IEEE Trans. Geosci. Remote Sens.*, vol. 60, pp. 1-16, 2022.

[4] S. Chen, X. Wang, S. Xiao, and M. Sato, *Target Scattering Mechanism in Polarimetric Synthetic Aperture Radar* Singapore: Springer, 2018.

[5] S. Chen, "Polarimetric coherence pattern: A visualization and characterization tool for PolSAR data investigation," *IEEE Trans. Geosci. Remote Sens.*, vol. 56, no. 1, pp. 286-297, 2018.

[6] S. W. Chen, X. S. Wang, and M. Sato, "Uniform Polarimetric Matrix Rotation Theory and Its Applications," *IEEE Trans. Geosci. Remote Sens.*, vol. 52, no. 8, pp. 4756-4770, 2014.

[7] M. Li, J. Deng, S. Xiao, and S. Chen, "NLSAN: A non-local scene awareness network for compact polarimetric ISAR image super-resolution," *IEEE Trans. Geosci. Remote Sens.*, vol. 61, pp. 1-16, 2023.

[8] S. Ren, K. He, R. Girshick, and J. Sun, "Faster R-CNN: Towards Real-Time Object Detection with Region Proposal Networks," *IEEE Trans. Pattern Anal. Mach. Intell.*, vol. 39, no. 6, pp. 1137-1149, 2017.

[9] X. Xie, G. Cheng, J. Wang, X. Yao, and J. Han, "Oriented R-CNN for Object Detection," presented at the 2021 IEEE/CVF International Conference on Computer Vision (ICCV), 2021.

[10] Y. Yu and F. P. Da, "Phase-Shifting Coder: Predicting Accurate Orientation in Oriented Object Detection," *2023 IEEE/CVF Conference on Computer Vision and Pattern Recognition (CVPR)*, pp. 13354-13363, 2022.

[11] C. Lyu, W. Zhang, H. Huang, Y. Zhou, Y. Wang, Y. Liu, *et al.*, "RTMDet: An Empirical Study of Designing Real-Time Object Detectors," *ArXiv*, vol. abs/2212.07784, 2022.

[12] C. A. Xu, H. Su, J. S. Li, Y. Liu, L. B. Yao, L. Gao, *et al.*, "RSDD-SAR: Rotated Ship Detection Dataset in SAR Images," *J. Radars*, vol. 11, no. 4, pp. 581–599, 2022.

[13] Z. Hong, X. Lei, W. Chao, W. Fan, and Z. Bo, "Investigation of the Capability of H-α Decomposition of Compact Polarimetric SAR," *IEEE Geosci. Remote Sens. Lett.*, vol. 11, no. 4, pp. 868-872, 2014.

[14] X. Yang, X. Yang, J. Yang, Q. Ming, W. Wang, Q. Tian, *et al.*, "Learning High-Precision Bounding Box for Rotated Object Detection via Kullback-Leibler Divergence," *ArXiv*, vol. abs/2106.01883, 2021.

[15] H. Zhu, "On Information and Sufficiency," *Working Papers*, vol. 157, no. 1, pp. 1–7, 1997.

[16] M. Li, X. Cui, C. Yang, S. Xiao, and S. Chen, "Polarimetric ISAR super-resolution based on group residual attention network," presented at the 2022 IEEE 10th International Conference on Information, Communication and Networks (ICICN), 2022.

[17] M. D. Li, S. P. Xiao, and S. W. Chen, "Pol-ISAR Space Target Component Salience Characteristic with Polarimetric Roll-Invariant Features," presented at the IET International Radar Conference, 2023.